Frequency-Domain Analytical Prediction of PWM-Induced Current Harmonics in Slotless Surface-Mounted PM Synchronous Machines

Xiaolong Zhang, *Member, IEEE,* Kiruba S. Haran, *Fellow, IEEE,* Philip T. Krein, *Fellow, IEEE,* and Luis J. Garcés

***Abstract*—Slotless surface-mounted permanent magnet synchronous machines with high pole numbers generally have relatively low inductance, which will lead to significant current harmonics under PWM-driven inverters. Current harmonics can cause additional losses and torque ripples, severely impacting temperature rises and mechanical vibrations. Accurate prediction of current harmonics is crucial for machine performance calculation and drive system design. This paper proposes a frequency-domain analytical method to predict the current harmonics with high fidelity equivalent circuit models. The harmonic prediction method is validated experimentally under a wide range of operating conditions and improves the prediction accuracy by up to 75% compared to the existing analytical modeling methods. The prediction error using the proposed method is generally maintained below 10%, making it an effective tool for practical applications.**

***Index Terms*—PM machines, pulse width modulation, carrier harmonics, total harmonic distortion, equivalent circuit**

I. Introduction

RAPID development of electrified transportation has stimulated an increasing demand for surface-mounted permanent magnet synchronous machines (PMSMs) [1]. The application of high-pole-number slotless designs has facilitated their continuous development towards high efficiency and high power density. Many research works have been published in recent years on their topology comparisons, electromagnetic and mechanical design, analysis and optimization [2]–[7]. In particular, drive and control of slotless SPM machines have been a research focus due to their inherent low inductance and current harmonic issues [8]–[12]. The high-frequency pulse-width modulation (PWM) harmonics introduced by the inverter could impose significant losses on the motor, leading to a decline in efficiency and winding insulation life. The implementation of filters to mitigate these harmonics not only adds extra weight and loss, but also amplifies the risks of reliability. Therefore, accurate analysis and prediction of PWM current harmonics are imperative to enhancing the slotless SPM motor system performance.

In order to estimate the harmful effects of harmonic phenomena, many current harmonics prediction methods have been developed [12]–[27], as summarized in TABLE I. According to the modeling methodology, they can be categorized into four different types. Specifically, machines can be modeled in the time domain or frequency domain. Furthermore, they can be expressed as equivalent circuit models or electromagnetic field models. Then, according to the computational method that solves the model, each type may have numerical and analytical alternatives.

TABLE I
Current Harmonics Prediction Method Summary

	Time-domain (time stepping)	Frequency-domain
Field model	Numerical: Yamazaki [13]– [14], Cheng [15], Jeong [16], Sarigiannidis [17] Analytical: Sprangers [18]	Sprangers [18] Jumayev [19]
Circuit model	Numerical: Leandro [12], Smith [20], Chiodetto [21], Zuo [22] Analytical: Ou [23], Chang [24]	Park [25] Liang [26]– [27]

In [13]–[15], precalculated PWM voltage waveforms were imported into time-stepped nonlinear finite element (FE) models to generate predicted non-sinusoidal current waveforms, thus calculating the losses in Interior Permanent Magnet (IPM) motors. In [16], [17], current control algorithm, PWM generation module, inverter circuit model, and motor finite element model were coupled together to obtain the PWM current harmonics and losses in IPM motors. The advantage of these FE methods is their high modeling fidelity in magnetic saturation and eddy current effects. However, building and solving FE models with solid conductor regions is quite time-consuming, therefore more computationally efficient method is desired.

To reduce computation time, the motor's electromagnetic field finite element model can be replaced with a subdomain-based electromagnetic field analytical model. [18] first used this method for calculating harmonic currents in induction motors and developed both time-domain and frequency-domain approaches. [19] applied the frequency-domain method to calculate harmonic currents and losses in a 2-pole SPM motor, which simultaneously calculated the operational inductance. The advantage of using subdomain-based methods is a significant reduction in computation time compared to FE method. However, since the solving process involves numerical iteration to inverse a large matrix constructed from the magnetic field boundary conditions, it remains a numerical rather than an analytical method.

Equivalent circuit modeling is another method to improve computational efficiency, comprising numerical and analytical

approaches. Numerical methods include those used by [12], [20]–[22]. They numerically solve simple motor RL series equivalent circuits to obtain current waveforms and then calculate the harmonics. The advantage of this method is its simplicity and fast solving speed, but it does not consider motor saturation effects and additional losses, leading to large prediction errors. In [22], flux-linkage lookup tables with saturation information were used to replace the constant L parameter to improve accuracy.

Analytical methods of equivalent circuit modeling have been presented in [23]–[27]. In [23], the motor is simplified as an equivalent L circuit, assuming that the ratio of the time-rate slope of the instantaneous current is constant. [24] used the same assumption but added a look-up table for L to include magnetic saturation and slotting effects in IPM motors. The advantage of this method is high computational efficiency. However, the constant slope assumption of the model significantly limits its universality. The various lossy components and reduced impedance at high frequencies are absent in the model, which may cause prediction errors. Moreover, the method cannot be extended to high-order circuits, such as drive circuits containing LC filters.

Instead of indirectly calculating spectrum from time-domain circuit solution as in [23]– [24], the amplitude of harmonic currents can be directly calculated in the frequency domain [25]–[27]. Frequency domain method is more straightforward because expressed in phasors, the harmonic current can be calculated by dividing harmonic voltage over the impedance. In [25], Park developed a frequency-domain equivalent circuit model, including LC filters, for synchronous reluctance motors in rotor reference frame to estimate rotor losses. However, the article did not provide any analytical voltage harmonic spectrum expressions. In [26]– [27], approximate analytical formulas for specific PWM sideband harmonics were derived. However, this approximate method cannot calculate all harmonic amplitudes and its equivalent circuit also neglect resistance components in the system.

Based on the above summary, we have identified two important aspects in the field of harmonic prediction that lack relevant research and need to be addressed. First, there is a lack of direct harmonic prediction formulas covering the entire frequency domain, Second, existing analytical equivalent circuit models generally used approximations that neglect resistance and rotor eddy current phenomenon including skin effects. To fill the gap, we propose an analytical method that directly calculates current spectral distribution in frequency domain. The proposed method further utilizes a high fidelity harmonic equivalent circuit that incorporates impedance-frequency characteristics in slotless SPM motors including rotor eddy current phenomenon and skin effects. Thus, the proposed method expands the state of the art in the following two aspects: First, the frequency-domain method provides explicit formulas for spectral distribution that covers all harmonics under different circuit topologies. This is a more direct and comprehensive computation of the harmonic distribution. Second, its equivalent circuit model considers eddy current phenomenon including skin effects, which are particularly significant factors in harmonic prediction when LC resonance is present or when voltage harmonic frequencies are high. This greatly improves prediction accuracy compared to the frequency-invariant circuit models used in existing methods

The paper is structured as follows. Section II details the frequency-domain harmonics prediction method. Section III presents the equivalent circuit model, including impedance-frequency characteristics of various circuit components. Section IV validates the proposed method through the experimental results and demonstrate the improved prediction accuracy compared to conventional frequency-invariant modeling method. A wide range of operating conditions is tested and carrier sideband harmonic distortion trends with regard to some key design parameters are demonstrated. Finally, conclusions are summarized in Section V.

II. Frequency-Domain Prediction Method

In this section, the concept of sequence harmonics is first introduced via "double decomposition analysis" process. Second, analytical expressions for positive- and negative-sequence harmonics is developed. Finally, the frequency-domain direct spectral prediction process using sequence harmonics is described.

A. Double Decomposition Analysis

To facilitate the use of equivalent circuit method, the current and voltage waveforms distorted by PWM processes should be transformed into a series of three-phase balanced quantities via "double decomposition analysis", whose processes is symbolically represented as (1) [28].

$$(t, y_a, y_b, y_c) \xrightarrow{\mathcal{F}} (h, \underline{Y}_a, \underline{Y}_b, \underline{Y}_c) \xrightarrow{\mathcal{T}} \left(\underline{Y}_{h+}, \underline{Y}_{h-}, \underline{Y}_{h0}\right) \quad (1)$$

Without loss of generality, assume there is a group of three-phase time series denoted as (t, y_a, y_b, y_c), where t is the time stamp. First, a Fourier transform (denoted as $\mathcal{F}$) is performed on each phase so that the time series is decomposed into frequency-domain harmonics. The harmonics from all three phases are organized as three phasor arrays labeled with the ordinal h, i.e., $(h, \underline{Y}_a, \underline{Y}_b, \underline{Y}_c)$. Then, a phase-sequence transform (denoted as $\mathcal{T}$) is performed for each individual harmonic order h, and a new set of harmonic phasors containing the positive-, negative- and zero-sequence components are obtained. These are called sequence-harmonics, whose ordinals are re-denoted as $h+$, $h-$, and $h0$, respectively. The phase-sequence transform for h-th harmonics can be expressed as

$$\begin{bmatrix} \underline{Y}_{h+} \\ \underline{Y}_{h-} \\ \underline{Y}_{h0} \end{bmatrix} = \underbrace{\frac{1}{3}\begin{bmatrix} 1 & \alpha & \alpha^2 \\ 1 & \alpha^2 & \alpha \\ 1 & 1 & 1 \end{bmatrix}}_{\mathcal{T}} \begin{bmatrix} \underline{Y}_{a,h} \\ \underline{Y}_{b,h} \\ \underline{Y}_{c,h} \end{bmatrix}, \quad (2)$$

where α is the 120° phase-shifting unit vector, defined as

$$\alpha = e^{j\frac{2\pi}{3}}. \quad (3)$$

The advantage of using sequence-harmonics for analysis is that each harmonic order corresponds to a set of three-phase

balanced ac voltages or currents at a particular frequency. Therefore, the three-phase circuit can be simplified and treated as a single-phase equivalent circuit. Once current sequence-harmonics are obtained, abc-phase current harmonic spectra and time-domain waveforms can be obtained by consecutively performing two inverse transformations, i.e., $\mathcal{T}^{-1}$ and $\mathcal{F}^{-1}$. For example, $\underline{Y}_{a,h}$ and y_a can be obtained by:

$$\begin{aligned} \mathcal{T}^{-1}: &\quad \underline{Y}_{a,h} = \underline{Y}_{h+} + \underline{Y}_{h-} + \underline{Y}_{h0} \\ \mathcal{F}^{-1}: &\quad y_a(t) = \sum_{h=0}^{\infty} \left|\underline{Y}_{a,h}\right| \cos\left(h\omega_1 t + \angle\underline{Y}_{a,h}\right). \end{aligned} \tag{4}$$

B. Closed-form Voltage Spectral Distribution Formulas

This section presents the double integral harmonic coefficients as introduced in [29], and derives the analytical expression for PWM voltage sequence harmonic spectrum. Some useful conclusions about PWM voltage spectral distribution characteristics are obtained.

In [29], voltage harmonic is analytically calculated with the double integral Fourier coefficients A_{mn}, where m is the carrier index variable, and n is the baseband index variable. These index variables define the frequency of each harmonic component of the switched phase leg output voltage, as $(mf_c + nf_o)$, where f_c is the carrier frequency, f_o is the target fundamental frequency. In other words, the nth sideband harmonic in the group of harmonics that are located around the mth carrier harmonic (i.e., within the second carrier sideband group) has a harmonic coefficient of A_{mn}.

For commonly used PWM algorithms, A_{mn} is explicitly expressed with m, n, as well as modulation index M and carrier ratio p, where

$$p = f_c/f_o. \tag{5}$$

For example, in the case of naturally sampled sinusoidal PWM (SPWM), A_{mn} takes a simple form when $m > 0$:

$$A_{mn} = \frac{4}{m\pi} J_n\left(m\frac{\pi}{2}M\right) \sin\left([m+n]\frac{\pi}{2}\right) \tag{6}$$

where J_n is the Bessel function of the first kind.

We can define a harmonic amplitude function $f(n) = |A_{mn}|$ for any given m. Since $J_{-n}(x) = (-1)^n J_n(x)$ when n is an integer, $f(n)$ is symmetric about the y-axis. This allows us to focus on the variation of $f(n)$ for $n > 0$. Fig. 1a plots the curves of $f(n)$ for M= 0.7, with different colors representing m = 1, 2, and 3, separately. The figure also shows the curve sampled at positive integers n, which are the harmonic amplitude values. Two features are identified. First, the envelope of $f(n)$ rapidly decays with increasing n, owing to the Bessel function term. Second, due to the modulation effect of the $\sin([m+n]\frac{\pi}{2})$ term, $f(n)$ is nonzero only when the parity of n and m is different (n is odd and m is even, or vice versa).

For the space vector PWM (SVPWM) scheme, we also have analytical expressions for A_{mn}, as listed in the Appendix. Fig. 1b illustrates the $f(n)$ curves for SVPWM, along with the integer-sampled bars representing actual harmonics. Like SPWM curves, $f(n)$ also decays when n increases. Generally,

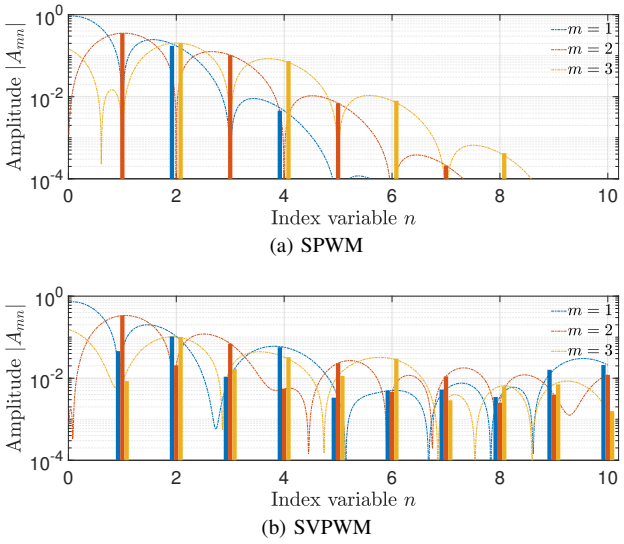

(a) SPWM

(b) SVPWM

Fig. 1. Variation of Harmonic Amplitude $|A_{mn}|$ with n

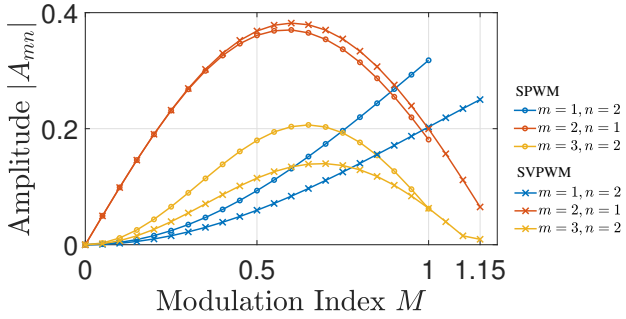

Fig. 2. Variation of Significant Harmonic Amplitude $|A_{mn}|$ with M

SVPWM has a wider spread of spectral distribution. When both n and m are odd or even, the harmonic may still exhibit small amplitude. However, both graph show that the second sideband harmonic of the first carrier group ($m = 1, n = 2$), the first sideband harmonic of the second carrier group ($m = 2, n = 1$), and the second sideband harmonic of the third carrier group ($m = 3, n = 2$), are generally the highest harmonic amid their respective carrier groups.

Next, let's examine the variation of $|A_{mn}|$ with M for these significant sideband harmonics. In Fig. 2, the amplitudes of these three most significant harmonics under SPWM and SVPWM schemes are plotted for M ranging from 0 to 1.15. It is observed that the first carrier sideband harmonic amplitude monotonically increases with increasing M, while the second and third carrier sideband harmonic amplitudes initially rise and then decline. The amplitude of the second carrier sideband harmonic is always greater than that of the third. This means that the first and second carrier harmonics have the highest amplitudes. When M is high, the first carrier sideband harmonic is greater than the second. When M is low, the second carrier sideband harmonic is greater than the second.

Fig. 3 compares the analytical prediction with the experimental measurement of the line-line PWM voltage for $M = 0.7$, $p = 20$ and $V_{dc} = 60$ V. It can be seen

This article has been accepted for publication in IEEE Transactions on Energy Conversion. This is the author's version which has not been fully edited and content may change prior to final publication. Citation information: DOI 10.1109/TEC.2023.3337191

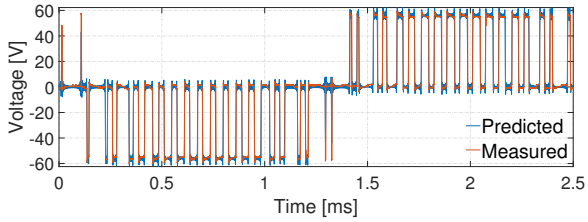

(a) Predicted and Measured Waveforms

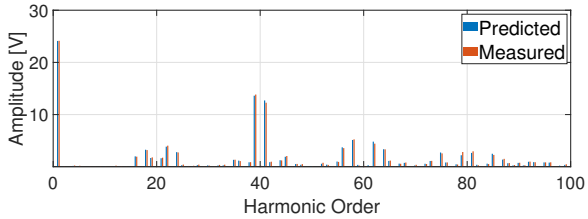

(b) Predicted and Measured Spectra

Fig. 3. Predicted and Measured Line-line Voltage Waveforms and Spectra for $V_{dc} = 60$ V, $M = 0.7$ and $p = 20$

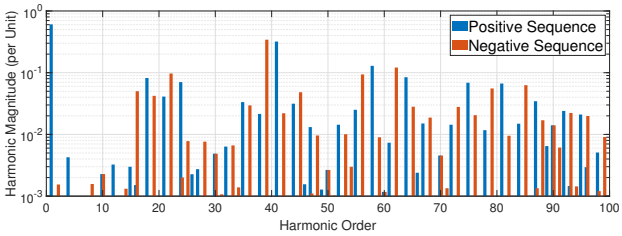

Fig. 4. Voltage sequence spectrum

from the waveforms and spectra that the two match well and the harmonic distribution aligns with the aforementioned characteristics. Some small discrepancies can be attributed to the non-linear factors in the actual hardware, such as switch device resistance, turn on/off delay and overshoot, non-ideal dead time effect, and close-loop controller influence. Some practical factors in the inverter can be modeled with adapted expressions of A_{mn}. For example, Dc bus voltage ripples may be considered using the analytical derivations presented in [30]. Analytical harmonic coefficients accounting for dead time effects are provided in [31].

Next, we can derive the expressions for positive, negative, and zero sequence voltages. We can obtain the voltage expressions for the abc phase as follows:

$$\begin{aligned} v_{sa} &= \frac{V_{DC}}{2} \sum_{m=0}^{\infty} \sum_{n=-\infty}^{\infty} A_{mn} \cos\left([m\omega_c + n\omega_o]\, t + m\theta_c + n\theta_o\right), \\ v_{sb} &= \frac{V_{DC}}{2} \sum_{m=0}^{\infty} \sum_{n=-\infty}^{\infty} A_{mn} \cos\left([m\omega_c + n\omega_o]\, t + m\theta_c + n\left[\theta_o - \frac{2\pi}{3}\right]\right), \\ v_{sc} &= \frac{V_{DC}}{2} \sum_{m=0}^{\infty} \sum_{n=-\infty}^{\infty} A_{mn} \cos\left([m\omega_c + n\omega_o]\, t + m\theta_c + n\left[\theta_o + \frac{2\pi}{3}\right]\right), \end{aligned} \tag{7}$$

where V_{dc} is the constant dc bus voltage, θ_c and θ_o are the initial phase angles of carrier and reference waveform signals, respectively. Angular frequencies ω_c and ω_o are defined by

$$\begin{aligned} \omega_c &= 2\pi f_c, \\ \omega_o &= 2\pi f_o. \end{aligned} \tag{8}$$

Combining (7) with (2), we can see that when n is equal to $3k+1$ for any integer k, it corresponds to positive sequence harmonic; when n is equal to $3k-1$, it corresponds to negative sequence harmonic; and when n is a multiple of three ($n = 3k$), it corresponds to zero sequence harmonic. In phasor form, the amplitudes of hth positive, negative, and zero sequence voltage harmonics can be synthesized from all harmonic coefficients following the above rules, i.e.,

$$\begin{aligned} \underline{V}_{s,h+} &= \frac{V_{DC}}{2} \sum_{m=0}^{\infty} \sum_{n=-\infty}^{\infty} A_{mn} e^{j[m\theta_c + n\theta_o]} \Big|_{\substack{mp+n=h \\ n=3k+1}} \\ \underline{V}_{s,h-} &= \frac{V_{DC}}{2} \sum_{m=0}^{\infty} \sum_{n=-\infty}^{\infty} A_{mn} e^{j[m\theta_c + n\theta_o]} \Big|_{\substack{mp+n=h \\ n=3k-1}} \\ \underline{V}_{s,h0} &= \frac{V_{DC}}{2} \sum_{m=0}^{\infty} \sum_{n=-\infty}^{\infty} A_{mn} e^{j[m\theta_c + n\theta_o]} \Big|_{\substack{mp+n=h \\ n=3k}} \end{aligned} \tag{9}$$

Thus, $\mathcal{F}$ and $\mathcal{T}$ transforms in (1) has been done analytically, and the tedious numerical calculation is skipped. Based on the earlier discussion, we can deduce the following characteristics of the voltage sequence harmonic spectrum:

1) High-amplitude harmonics are concentrated around integer multiples of the carrier frequency. Harmonics within a single carrier sideband group exhibit a decreasing trend away from the center carrier harmonic.
2) Generally, harmonics corresponding to odd m / even n or even m / odd n combinations have relatively high amplitudes. For instance, within the first carrier sideband group, significant harmonics occur at $p\pm2$, 4, 6, etc. Within the second carrier sideband group, significant harmonics occur at $2p\pm1$, 3, 5, etc.
3) Each harmonic can be further classified into positive, negative, and zero sequence harmonics based on the remainder when dividing n by 3. For example, $p-2$, $p+4$ have dominant positive sequence component; $p+2$, $p-4$ have dominant negative sequence component; $p\pm6$ have dominant zero sequence component. In the spectrum diagram, positive, negative, and zero sequence harmonics tend to occupy alternate ordinal numbers.

Fig. 4 illustrates the theoretically calculated positive and negative sequence voltage harmonic spectra for a two-level inverter controlled by a SVPWM scheme with $M = 0.7$ and $p = 20$. Since the neutral point of the motor is generally not grounded and there is no path for zero-sequence current, the zero-sequence voltage harmonics are out of our interest and therefore not shown here.

C. Frequency-Domain Current Harmonic Prediction

The process of frequency-domain prediction method for current harmonics is summarized in Fig. 5. First, the voltage sequence harmonic spectrum is analytically determined based on the inverter topology and PWM scheme. Second, based on the distribution of harmonic frequencies, the equivalent circuit parameters for the positive and negative h-th order harmonics are obtained, and the impedance expressions should be calculated. Third, each voltage sequence-harmonic is divided by

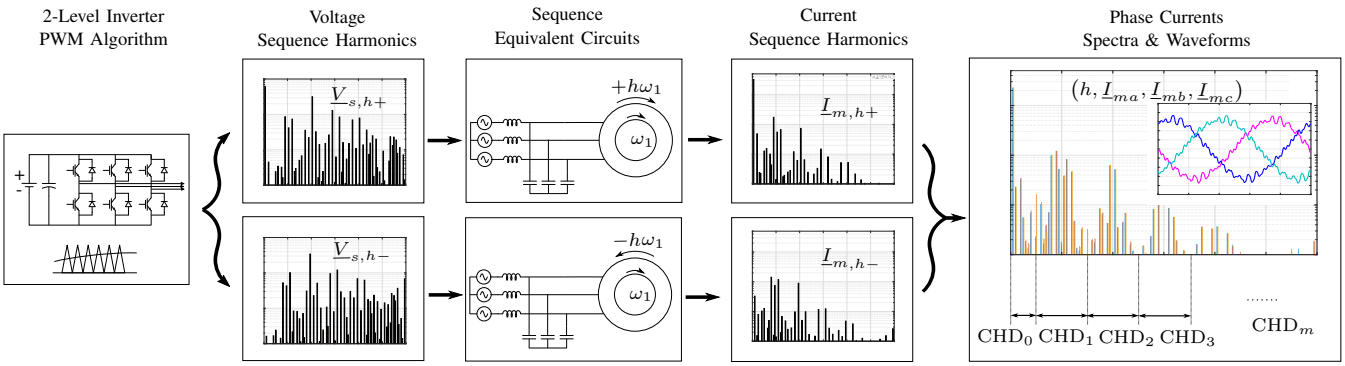

Fig. 5. Current harmonics prediction flowchart

its corresponding impedance to obtain the current sequence-harmonic, i.e.,

$$\underline{I}_{m,h\pm} = \frac{\underline{V}_{s,h\pm}}{\underline{Z}_{t,h\pm}}. \tag{10}$$

Finally, we can convert the 120 sequence currents into abc phase current quantities for all harmonic orders using (11).

$$\begin{bmatrix} \underline{I}_{ma,h} \\ \underline{I}_{mb,h} \\ \underline{I}_{mc,h} \end{bmatrix} = \underbrace{\begin{bmatrix} 1 & 1 & 1 \\ \alpha^2 & \alpha & 1 \\ \alpha & \alpha^2 & 1 \end{bmatrix}}_{\mathcal{T}^{-1}} \begin{bmatrix} \underline{I}_{m,h+} \\ \underline{I}_{m,h-} \\ \underline{I}_{m,h0} \end{bmatrix} \tag{11}$$

In general, obtaining the harmonic spectrum of the three-phase current is sufficient for machine performance prediction such as electromagnetic loss or torque ripple, and there is no need to continue calculating the time-domain expression. Furthermore, only harmonics within a certain bandwidth are necessarily computed. Usually, harmonics beyond $4f_c$ contribute very little to electromagnetic losses or torque ripples. As a result, the number of harmonics (in the order of tens or hundreds) to be calculated in a frequency-domain method is much smaller than the number of time steps (typically tens of thousands) required in a time-stepping method, which leads to significantly reduced computation time.

Once the current harmonic spectrum is obtained, it is easy to calculate total harmonic distortion (THD). Here, we introduce a new set of parameters indicating the combined amplitude of the sideband harmonics near a certain carrier harmonic. By definition, m-th carrier sideband-harmonic-group distortion (CHD_m) is

$$\mathrm{CHD}_m = \frac{\sqrt{\sum_{(m-\frac{1}{2})p<h\leq(m+\frac{1}{2})p} \hat{\underline{I}}_h^2}}{\hat{\underline{I}}_1}. \tag{12}$$

For completeness, the baseband-harmonic-group distortion (CHD_0) is also defined and expressed as

$$\mathrm{CHD}_0 = \frac{\sqrt{\sum_{1<h\leq\frac{p}{2}} \hat{\underline{I}}_h^2}}{\hat{\underline{I}}_1}. \tag{13}$$

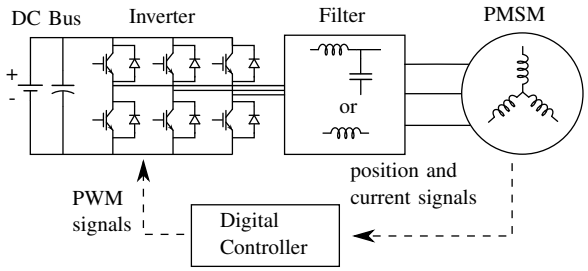

Fig. 6. PMSM Variable Speed Drive System

The span of these harmonic groups is illustrated in the last graph of Fig. 5. THD can be found through the squared sum of CHD_m, i.e.

$$\mathrm{THD} = \sqrt{\sum_{m=0}^{\infty} \mathrm{CHD}_m^2}. \tag{14}$$

Compared to THD, CHD_m reveals the important frequency distribution of harmonic spectra and can help us better understand the trend of harmonic distortion changes with respect to drive system parameters.

III. Slotless SPM Equivalent Circuit Model

A crucial step in the frequency-domain prediction is the development of sequence harmonic equivalent for the machine drive system, which includes an inverter, a dc bus, a possible filter, and a surface-mounted PMSM, as shown in Fig. 6. This section is dedicated to such a model that includes the impedance-frequency curves of the machine and filter. Analytical expressions will be presented to illustrate their trends. We assume that the dc values of the circuit components are known through FE simulation and focus on the increment of the ac value as the frequency changes.

A. Equivalent Circuit Model for Sequence-Harmonics

The drive-system model includes two types of per-phase lumped-parameter equivalent circuits separately for fundamental harmonic and asynchronous sequence-harmonics, as shown

This article has been accepted for publication in IEEE Transactions on Energy Conversion. This is the author's version which has not been fully edited and content may change prior to final publication. Citation information: DOI 10.1109/TEC.2023.3337191

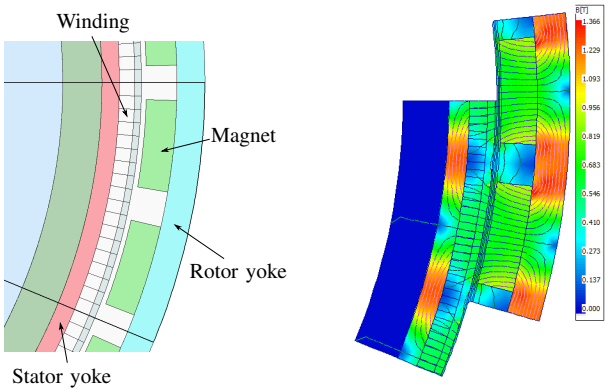

(a) Design Cross Section (b) FE Model

Fig. 7. Slotless SPM Machine

TABLE II
SLOTLESS SPM MACHINE GEOMETRICAL PARAMETERS

Parameter	Unit	Value
Pole number		32
Slot per pole per phase		3
Rotor back iron thickness	mm	4
Magnet thickness	mm	4.3
Magnet width	mm	12.4
Magnet type		NdFeB
Stator OD	mm	172.1
Airgap	mm	0.7
Winding thickness	mm	3.1
Stator back iron thickness	mm	2.5

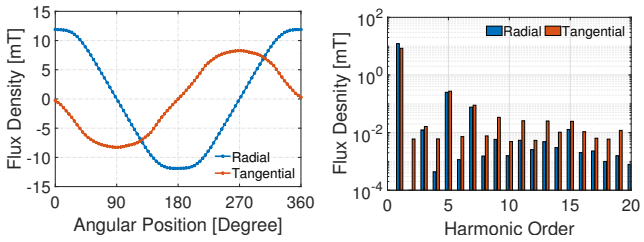

(a) Spatial waveform (b) Spatial spectrum

Fig. 8. Armature Reaction Field in the Airgap

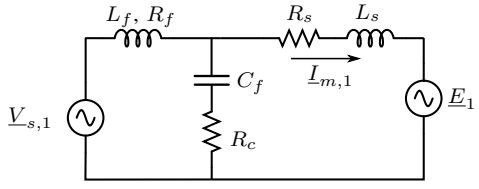

(a) For Fundamental Harmonic

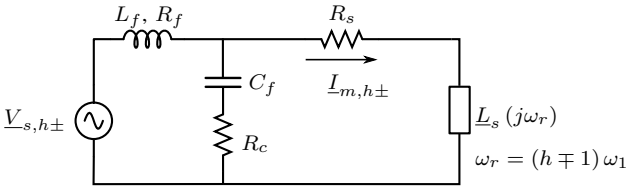

(b) For Asynchronous Sequence-Harmonics

Fig. 9. Machine Per-phase Equivalent Circuit Model

in Fig. 9. Each circuit must have three parts modeled, i.e., inverter, filter and machine.

The inverter is represented as a voltage source in each circuit. The fundamental voltage harmonic, and positive- or negative-sequence h-th asynchronous voltage harmonics are symbolized as $\underline{V}_{s,1}$ and $\underline{V}_{s,h\pm}$, respectively. In Section II-B, the determination of these voltage harmonic components have been presented.

Assume an LC filter is used between the inverter and the motor to reduce the high-frequency harmonic contents. The associated circuit parameters include the inductance (L_f) and resistance (R_f) of the inverter-side inductor, the capacitance of the shunt capacitor (C_f), and the damping resistor (R_c) in series with the capacitor.

Now our focus will be the slotless SPM machine equivalent circuits. The establishment of this equivalent circuit is based on the following assumptions:

1) The armature reaction magnetic field in the airgap is a sine wave, and the harmonic leakage component in the magnetizing inductance can be neglected.
2) The saturation effect on the motor inductance can be neglected, and the synchronous inductance does not significantly change with the load current or rotor position.

These assumptions are true due to the very large electromagnetic airgap in this machine class. We took a commercial off-the-shelf slotless outer-rotor SPM motor shown in Fig. 7a as an example and established a finite element model to numerically calculate the magnetic field distribution and inductance. Its geometrical details are tabulated in TABLE II. Fig. 8a shows the radial and tangential components of the armature reaction field in the air gap region versus rotor position. Fig. 8b shows the corresponding spatial harmonic spectrum. Due to the relatively large electromagnetic airgap, the armature reaction field is low, with radial and tangential fundamental components of only 12.2 mT and 8.4 mT, respectively. The spectral analysis results show that the high-order spatial harmonic components are even lower. The THD of the radial and tangential magnetic fields is only 2.2% and 3.5%, respectively. Since inductance is proportional to the square of the magnetic field magnitude, the harmonic inductance accounts for less than 0.1% of the overall magnetizing inductance, which is negligible from an impedance point of view. This means that for a three-phase balanced current excitation of any particular frequency, the armature reaction field in the air gap can be considered as a sine wave with a spatial period of p and a fixed rotating speed proportional to the excitation frequency.

TABLE III lists the synchronous inductance at different

TABLE III
VARIATION RANGE OF INCREMENTAL SYNCHRONOUS INDUCTANCE OVER DIFFERENT ROTOR POSITIONS AND CURRENT AMPLITUDES

Current amplitude	FE Incremental Synchronous inductance over different rotor positions [uH]
0A	12.3-12.5
5A	12.3-12.5
10A	12.3-12.5
15A	12.3-12.5
20A	12.3-12.5

current amplitudes and rotor positions. Two steps were taken to derive the synchronous inductance L_s. First, incremental phase self-inductance and mutual inductance are calculated in the FE model. Than the synchronous inductance is obtained using the following formula:

$$L_s(\theta) = L_{AA} - \frac{M_{AB} + M_{AC}}{2} \tag{15}$$

Where θ is the rotor position, L_{AA} is the self-inductance of phase A winding, M_{AB} is the mutual inductance between phases A and B, and M_{AC} is the mutual inductance between phases A and C, all of which are dc incremental values. It can be seen that due to the large equivalent air gap in the slotless SPM, the inductance barely changes with the current amplitude or rotor position. Thus, a series circuit comprising the phase resistance and a complex-valued inductance can represent the machine impedance at any particular stator frequency.

First, the fundamental-harmonic circuit, as shown in Fig. 9a, addresses only the synchronous-frequency ($\omega_1 = 2\pi f_o$) current. The machine is represented as a serial connection of the synchronous inductance L_s, stator resistance R_s and back electromotive force (EMF) $\underline{E}_1$. This is the classical synchronous machine steady-state equivalent circuit, which can be used to determine the fundamental voltage phasor $\underline{V}_{s,1}$. Then, M and θ_o can be determined according to

$$M = \frac{2\hat{\underline{V}}_{s,1}}{V_{dc}}, \tag{16}$$

$$\theta_o = \angle \underline{V}_{s,1}. \tag{17}$$

The equivalent circuits for higher-order sequence-harmonics are developed considering stator asynchronous fields, as shown in Fig. 9b. The machine impedance is determined by an equivalent circuit consisting of serially-connected stator resistance R_s and complex-valued operational inductance $\underline{L}_s(j\omega_r)$. The concept of operational inductance will be explained in more detail in Section III-C. The slip frequency ω_r is needed to determine its value for each sequence-harmonic.

For a particular h, the slip frequency corresponding to the positive- and negative- sequence-harmonic currents are different. The magneto-motive force (MMF) induced by the positive-sequence currents rotates in the positive direction at a speed proportional to its electrical frequency $h\omega_1$. The MMF induced by negative-sequence currents rotates at the same speed but in the opposite direction, corresponding to an electrical frequency $-h\omega_1$. The MMF induced by the zero sequence current, if it exists, remains stationary. Unless the winding neutral is connected to the ground, there will be no zero-sequence currents. The electrical frequency of the induced currents in the rotor circuit is the slip frequency ω_r, which is determined by the relative speed between the stator MMF traveling wave and the rotor. The rotor is spinning at the synchronous frequency ω_1 at the steady state. Thus, the slip frequency for the positive-sequence h-th harmonic component is $(h-1)\omega_1$; the slip frequency for the negative-sequence h-th harmonic component is $(h+1)\omega_1$. In summary, for any sequence harmonic ordinal $h\pm$, the slip frequency, or rotor circuit frequency, can be expressed as

$$\omega_{r,h\pm} = (h \mp 1)\,\omega_1. \tag{18}$$

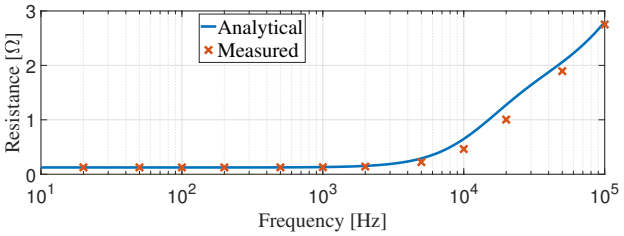

Fig. 10. Resistance of a 306 μH Inductor

Then the operational inductance $\underline{L}_s$ in the equivalent circuits is determined by evaluating the $\underline{L}_s(j\omega_r)$ characteristic curve at $\omega_{r,h\pm}$. An equivalent-circuit model to compute $\underline{L}_s$ characteristic curve is described in Section III-C.

B. Resistance of Multi-Strand/Multi-Turn Coils

In the windings of magnetic components such as inductors, transformers, and motors, the structure of multi-strand/multi-turn coils is widely used. Due to the presence of alternating leakage fields, the current in each strand or turn of the coil exhibits an uneven distribution, resulting in the phenomenon that ac resistance is greater than dc resistance, known as proximity/skin effects. Generally, the higher the frequency, the greater the ac resistance. Assuming that the leakage field is distributed in a parallel manner in the winding area, one can calculate ac resistance with the following equations [32], [33]:

$$\xi_c(\omega) = h_c\sqrt{\omega\mu_0\sigma_c\frac{b_c}{2b}}, \tag{19}$$

$$\varphi(\xi_c) = \xi_c\frac{\sinh(2\xi_c)+\sin(2\xi_c)}{\cosh(2\xi_c)-\cos(2\xi_c)}, \tag{20}$$

$$\psi(\xi_c) = 2\xi_c\frac{\sinh(\xi_c)-\sin(\xi_c)}{\cosh(\xi_c)+\cos(\xi_c)}, \tag{21}$$

$$k_R(\xi_c) = \varphi(\xi_c) + \frac{z_t^2-1}{3}\psi(\xi_c), \tag{22}$$

$$R_{ac} = k_R(\xi_c)\,R_{dc}, \tag{23}$$

where h_c is the strand/turn height, σ_c is the wire conductivity, b_c is the wire width, b is the width between iron core walls, z_t is the number of layers in perpendicular to the leakage flux, ξ_c is called the reduced conductor height, k_R is called the ac resistance factor. When the frequency is high ($\xi_c > 2$), k_R will increase proportionally with ξ_c, i.e., at a rise rate of $\omega^{\frac{1}{2}}$.

In general, R_f and R_s in the equivalent circuit model follows this frequency dependency trend. Fig. 10 plots the predicted and measured resistance value of a 306 μH multi-turn inductor versus excitation frequency, which consolidates the analytical expression.

C. Operational Inductance

As the eddy current density in the rotor conductive parts such as magnets changes with frequency, the motor impedance also changes with frequency. We can study the trend of impedance variation using equivalent circuits.

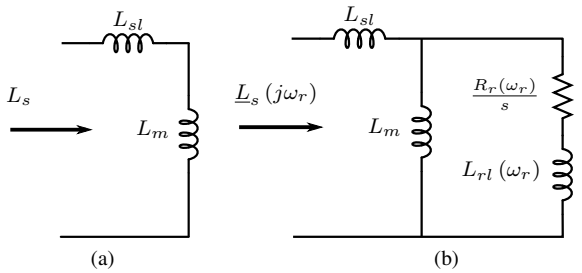

Fig. 11. Equivalent Circuits for Motor Inductance: (a) synchronous inductance, (b) operational inductance

First, consider the simplest, fundamental-harmonic case where the stator field is synchronous with the rotor. The armature reaction field is stationary with respect to the rotor, so there is no induced eddy current in the magnets. The motor impedance consists only of the magnetizing inductance L_m and the stator leakage inductance L_{sl}, as shown in Fig. 11a. The lumped inductance is the synchronous inductance L_s.

Now, let's consider a stator excitation of an arbitrary asynchronous frequency $\omega_h(\neq \omega_1)$. Eddy currents are induced in the rotor magnets as the slip between stator-excited field and the spinning rotor appears. The magnetic field generated by the eddy current generally weakens the original air gap magnetic field according to Lenz's law, thereby reducing the motor inductance. In addition, eddy currents flowing in the rotor magnets with non-zero conductivity will generate Joule losses. The impedance seen from the stator winding ports not only have a reactive component but also a resistive lossy component. These effects grow stronger as the slip frequency between the stator and rotor (which is the frequency of rotor eddy currents, ω_r) increases. In summary, the motor impedance under asynchronous stator current excitation is a complex function that varies with the slip frequency. It is characterized by the so-called operational inductance, $\underline{L}_s(j\omega_r)$.

The operational inductance can be represented by an equivalent circuit that comprises additionally a rotor branch connected in parallel to the magnetizing inductance [34]–[36], as shown in Fig. 11b. The added branch includes a rotor resistance R_r and a rotor leakage inductance L_{rl}. R_r is divided by the slip s to account for the frequency difference between stator and rotor currents, where s is expressed as

$$s = \omega_r/\omega_h. \tag{24}$$

Through simple manipulation of impedance expression from Fig. 11b, the operational inductance is obtained as

$$\underline{L}_s(j\omega_r) = L_m \frac{R_r + j\omega_r L_{rl}}{R_r + j\omega_r(L_{rl} + L_m)} + L_{sl}. \tag{25}$$

Rare earth permanent magnet materials exhibit significant skin effects under high-order harmonics due to their low resistivity and significant geometrical size. When the frequency increases, the eddy current density increases, while the penetration depth decreases, which is similar to the deep bar effects in an induction machine (IM) [37]. Just like an IM, R_r and L_{rl} of an SPM motor also change with rotor frequency ω_r. The direct cause of the parametric variation is the circulating current induced by the alternating magnetic field that penetrates the conductor. Figs. 12a and 12b respectively illustrate the alternating magnetic flux lines on the rotor bar in IM and the permanent magnet in SPM, as well as the distribution of the induced circulating currents. As the frequency increases, the circulating currents tend to concentrate on the surfaces of the conductor parallel to the magnetic flux lines with a certain skin depth. Again, we can define the reduced conductor height ξ_m to characterize the skin effect:

$$\xi_m(\omega_r) = h_m\sqrt{\omega_r\mu_m\sigma_m\frac{b_m}{2g'}}, \tag{26}$$

where h_m is the magnet circumferential width, b_m is the magnet width, σ_m is the magnet conductivity, μ_m is the magnet permeability, g' is the electromagnetic airgap length (equals to the physical airgap plus the magnet depth).

Based on the similarity between the magnetic field and circulating current distribution, we can assume that the frequency-dependency functions of R_r and L_{rl} of the permanent magnet follows a pattern similar to that of the deep bar conductor in IM [38], i.e.,

$$R_r = \xi_m\frac{\sinh(2\xi_m)+\sin(2\xi_m)}{\cosh(2\xi_m)-\cos(2\xi_m)}R_{r0}, \tag{27}$$

$$L_{rl} = \frac{3}{2\xi_m}\left(\frac{\sinh(2\xi_m)-\sin(2\xi_m)}{\cosh(2\xi_m)-\cos(2\xi_m)}\right)L_{rl0}, \tag{28}$$

where R_{r0} and L_{rl0} are the dc values of these parameters. Both of these dc parameters are determined by the net current distribution (not the circulating current) on the conductor's cross-section and the induced magnetic flux, which will be affected by the external magnetic circuit. Even though (27) and (28) can be used as good approximation formulas for frequency effects, analytical expression of R_{r0} and L_{rl0} for the deep bar conductor cannot be directly applied. Their values in SPM machines can be determined by FE methods.

As expected, (27) and (28) suggest that R_{r0} increases while L_{rl0} decreases as ω_r increases. When ω_r is high ($\xi_m > 2$), R_{r0} and L_{rl0} change approximately in the order of $\omega_r^{\frac{1}{2}}$ and $\omega_r^{-\frac{1}{2}}$, respectively.

In Fig. 13, real and imaginary parts of $\underline{L}_s(j\omega_r)$ of the Thingap surface-mounted PMSM are calculated by the analytical equivalent circuit model. The real part corresponds to the inductive component, while the imaginary part corresponds to the resistive component. The real part is always positive and monotonically decreases with frequency. The imaginary part is always negative owing to real power consumption, and its absolute value first increases and then decreases with the frequency. The analytical results are validated by motor impedance measurements with an HP 4284A Precision LCR meter and good agreement is found. Some small discrepancies may be attributed to the distributed parasitic circuit parameters.

D. Positive and Negative Sequence Equivalent Impedance

Once we obtain the impedance-frequency characteristic curves of each component, we can then calculate the equivalent impedance required by (10). Based on the circuit model in

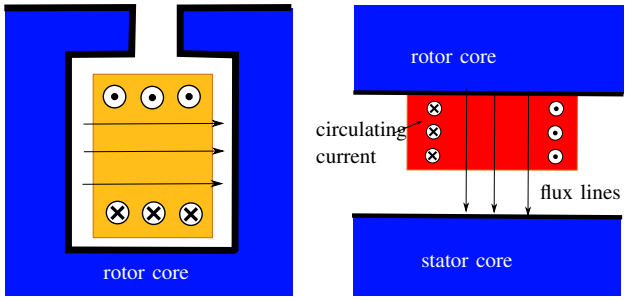

(a) Induction motor (b) SPM motor

Fig. 12. Alternating flux lines and induced circulating currents in rotor conductive parts

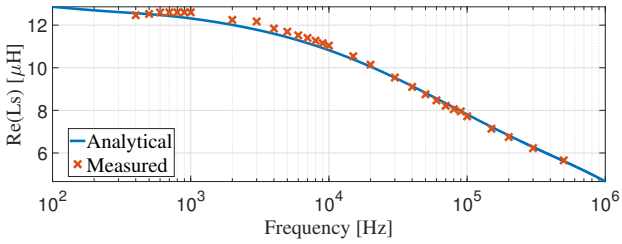

(a) Re $(\underline{L}_s)$

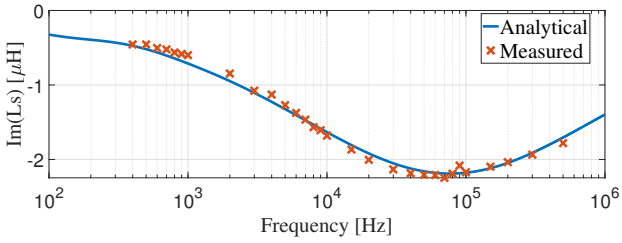

(b) Im $(\underline{L}_s)$

Fig. 13. Operational Inductance $(\underline{L}_s)$ vs Frequency

Fig. 9b, the Thevenin equivalent impedance $\underline{Z}_t$ for the harmonic ordinal $h\pm$ is derived in (29) to calculate the machine harmonic current excited by a particular voltage harmonic:

$$\begin{aligned}\underline{Z}_{t,h\pm} &\overset{\text{def}}{=} \frac{\underline{V}_{s,h\pm}}{\underline{I}_{m,h\pm}} \\ &= R_f + R_s + j\left(X_f + \underline{X}_s\right) + \frac{\left(R_f + jX_f\right)\left(R_s + j\underline{X}_s\right)}{R_c - jX_c},\end{aligned} \tag{29}$$

where the impedance are given by

$$\begin{aligned} X_f &= \omega_h L_f, \\ \underline{X}_s &= \omega_h \underline{L}_s\left(j\omega_{r,h\pm}\right), \\ X_c &= \tfrac{1}{\omega_h C_f}, \end{aligned} \tag{30}$$

and the stator's harmonic frequency $\omega_h = h\omega_1$.

If we assume that all the resistance can be neglected and $\underline{L}_s \approx L_s$ at the resonant frequency f_{res}, then f_{res} can be obtained as approximately

$$f_{\text{res}} = \frac{1}{2\pi}\sqrt{\frac{L_s + L_f}{L_s L_f C_f}}. \tag{31}$$

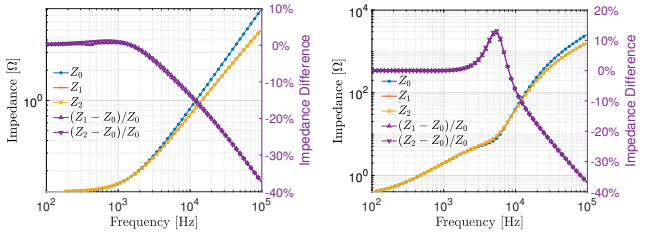

(a) Machine Impedance (b) Machine and LC Filter System Impedance

Fig. 14. Machine and system impedance under positive and negative sequence harmonics (Z_0: Impedance from frequency-invariant model, Z_1:Positive sequence impedance from proposed model, Z_2:Negative sequence impedance from proposed model)

TABLE IV
CIRCUIT PARAMETERS OF THE EXPERIMENTAL SYSTEM

Parameters	Unit	Value
Number of Poles		32
PM Flux Linkage per Phase	mWb	7.58
Synchronous Inductance, Ls	μH	12.4
Phase Resistance, R_s	$m\Omega$	125.2
Filter Inductance, L_f	μH	305
Filter Capacitance, C_f	μF	60
Damping resistance, R_c	Ω	0.2

Generally, filter parameters should be selected so that f_{res} resides between f_o and f_c. If an L filter is used instead of the LC filter, the impedance expression is simply:

$$\underline{Z}_{t,h\pm} = R_s + R_f + j\left(X_f + \underline{X}_s\right). \tag{32}$$

If no filter is used, then

$$\underline{Z}_{t,h\pm} = R_s + j\underline{X}_s. \tag{33}$$

Table IV provides an overview of the motor and filter system parameters used in this study.The filter inductance is set at 305 μH, whereas the filter capacitance is 60 μF, and the damping resistance is fixed at 0.2 Ω. The resonant frequency f_{res} is 5.6 kHz.

A review of previous literature has shown that the existing analytical models often assume frequency-invariant equivalent circuit parameters. Now, let's compare the proposed model and a frequency-invariant model and examine the change of the equivalent impedance when frequency factors are taken into account.

Firstly, consider the simplest scenario, where there is no filter and only the motor is present, represented by (33). The impedance corresponding to constant inductance, denoted as Z_0 $(= \omega_h L_s)$, the positive sequence impedance Z_1 $(= |\underline{Z}_{t,h+}|)$, the negative sequence impedance Z_2 $(= |\underline{Z}_{t,h-}|)$, and their percentage differences are illustrated in Fig. 14a. It can be observed that at lower frequencies, the positive and negative sequence impedances show no significant difference compared to the impedances calculated using the frequency-invariant model. However, as the frequency increases, differences gradually become pronounced, with the positive and negative sequence impedance being lower. Moreover, the

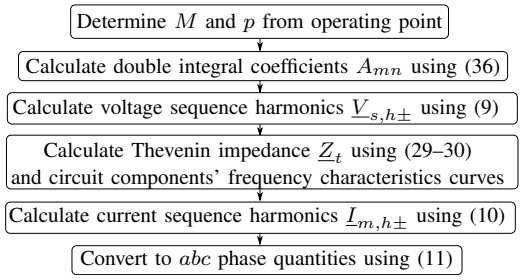

Fig. 15. Current Harmonic Spectrum Prediction Flowchart

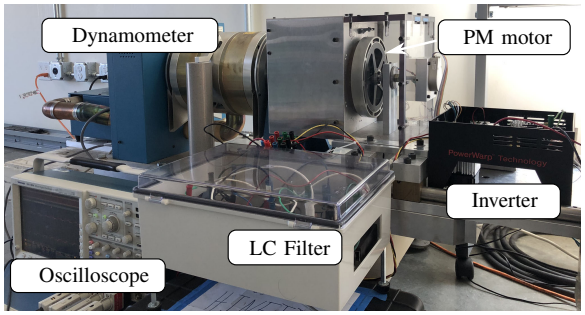

Fig. 16. Lab Experimental Setup

higher the frequency, the higher the percentage decrease in impedance.

Next, consider the LC circuit scenario represented by (29), and the curves are ploted in Fig. 14b. This situation is more complex than the previous one. The impedance characteristic curve is divided by f_{res} into two segments. Below f_{res}, the impedance is capacitive. Above f_{res}, the impedance becomes inductive. Around f_{res}, due to mutual cancellation between L and C, the impedance exhibits a significant dip, constituting primarily a resistive component.

As seen from the earlier discussion, the eddy current phenomenon including skin effects manifests in the lumped parameters primarily in two ways: firstly, by increasing the resistive impedance, and secondly, by causing a decrease in the inductive impedance. At low frequencies, Z_0, Z_1 and Z_2 show no significant difference, as the capacitance does not vary with frequency. When the frequency approaches the resonance point (5.6 kHz), the frequency effect leads to an increase in the equivalent impedance Z_1 and Z_2, which can reach up to 10%. As the frequency surpasses the resonance point to a certain extent, it induces a decrease in Z_1 and Z_2 compared to Z_0, and as the frequency increases, the impedance reduction becomes more pronounced. By the time we reach 40 kHz, impedance can be reduced by up to 20% compared to Z_0. From this, it becomes evident that neglecting the impedance-frequency characteristic curve can introduce significant errors in harmonic prediction.

Once the expression for $\underline{Z}_t$ is determined, we possess a set of analytical equations to determine the current harmonics. For instance, for a slotless SPM motor system with an LC filter and a 2-level inverter driven by SVPWM, equations (9), (10), (11), (29), (30), and (36) constitute a set of close-form prediction equations. They can be implemented using the flowchart in Fig. 15. In the following, we will use this process to predict current harmonic spectra for an experimental setup under various settings. The effectiveness of the proposed method is validated by comparing it against actual test results.

IV. Model Validation with Experimental Data Analysis

We will scrutinize the current harmonic spectra obtained from the model prediction and experimental results under various scenarios. The prediction errors from both the proposed method and the existing method that do not consider frequency-impedance characteristics are presented and compared.

A. Experimental Setup and Procedure

The experimental system hardware is shown in Fig. 16. It comprises the same slotless SPM motor (Brand name: ThinGap) as presented in the previous analysis. The inverter is a Texas Intrument's High Voltage Digital Motor Control and Power Factor Correction kit (Part Number: TMDSHVMTRPFCKIT). We ran the PM motor in speed control mode and regulated the current by synchronous PI control, using a symmetrical SVPWM algorithm. Furthermore, the dynamometer operated in torque mode and provided a load torque that kept the motor current at 4 A_{rms}. The instantaneous machine current signals were measured by Tektronix TCP0030A current probes with 1.5% accuracy, which were connected to a Tektronix Model MSO-4034 Oscilloscope. The oscilloscope recorded the data and stored them on a PC. We then performed an Fast Fourier Transform (FFT) on the saved data to obtain the harmonic spectrum.

We investigated how changes in carrier frequency f_c, dc bus voltage V_{dc}, filter capacitance C_f, and modulation index M affected the current harmonic spectrum, as predicted by our model, and compared the findings with the experimental results. Fig. 17 depicts the predicted and experimental spectra and waveforms of six representative testing cases. Fig. 18 illustrates the trends of CHD_0-CHD_2 with respect to the aforementioned operating parameters. We will discuss our observations in detail with these graphs in the rest of the section.

B. Carrier Frequency

An LC filter with 60 μF capacitance is used for studying the influence of f_c. A constant operating speed for the motor is maintained, which implies that f_o and back EMF amplitude remain unchanged. Additionally, we keep V_{dc} constant, which ensures that the modulation index M remains almost unchanged. At this point, we examine the spectral and waveform characteristics under two different f_c, as shown in Figs. 17a-17d. Here, we maintain that $f_o = 400$ Hz, $V_{dc} = 60$ V, and $M = 0.8$ for both cases, while their f_c are 5.6 kHz and 7.2 kHz, respectively, giving rise to p of 14 and 18 for each case.

It is observed that the higher the carrier frequency, the lower the amplitudes of the current harmonic components. This is

This article has been accepted for publication in IEEE Transactions on Energy Conversion. This is the author's version which has not been fully edited and content may change prior to final publication. Citation information: DOI 10.1109/TEC.2023.3337191

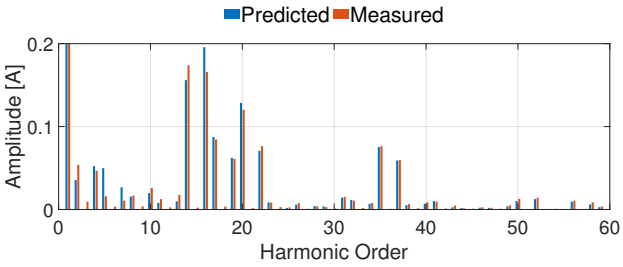

(a) Spectra: $f_o = 400$ Hz, $p = 18$, 60 μF, $V_{dc} = 60$ V, $M = 0.8$.

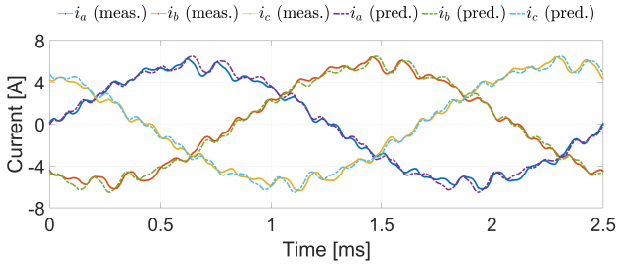

(b) Waveforms: $f_o = 400$ Hz, $p = 18$, 60 μF, $V_{dc} = 60$ V, $M = 0.8$.

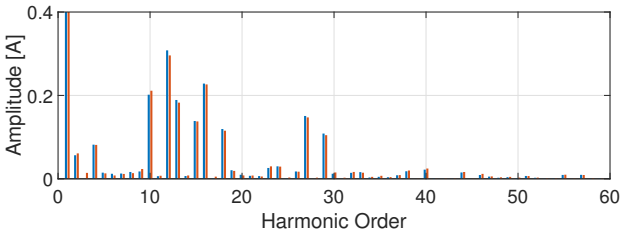

(c) Spectra: $f_o = 400$ Hz, $p = 14$, 60 μF, $V_{dc} = 60$ V, $M = 0.8$.

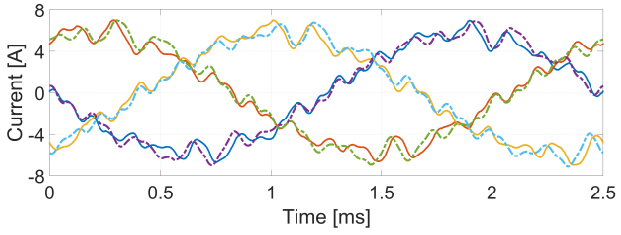

(d) Waveforms: $f_o = 400$ Hz, $p = 14$, 60 μF, $V_{dc} = 60$ V,$M = 0.8$.

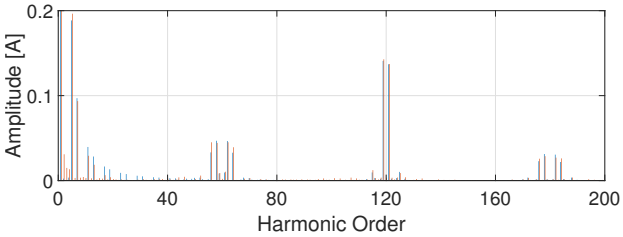

(e) Spectra: $f_o = 200$ Hz, $p = 60$, no C_f, $V_{dc} = 50$ V, $M = 0.55$.

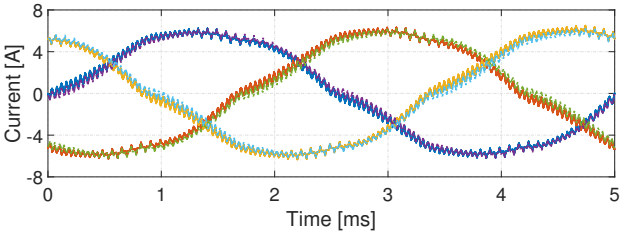

(f) Waveforms: $f_o = 200$ Hz, $p = 60$, no C_f, $V_{dc} = 50$ V, $M = 0.55$.

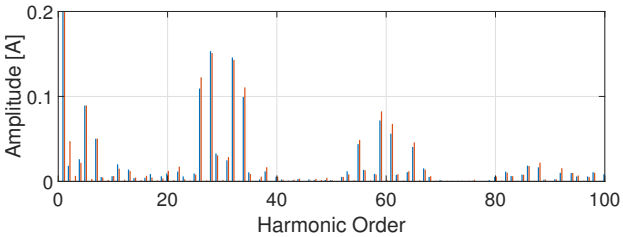

(g) Spectra: $f_o = 400$ Hz, $p = 30$, no C_f, $V_{dc} = 50$ V, $M = 1.0$.

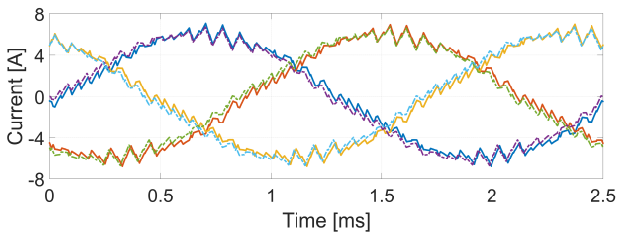

(h) Waveforms: $f_o = 400$ Hz, $p = 30$, no C_f, $V_{dc} = 50$ V, $M = 1.0$.

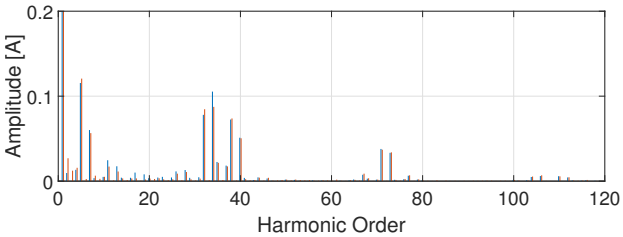

(i) Spectra: $f_o = 200$ Hz, $p = 36$, 60 μF, $V_{dc} = 33$ V, $M = 0.8$.

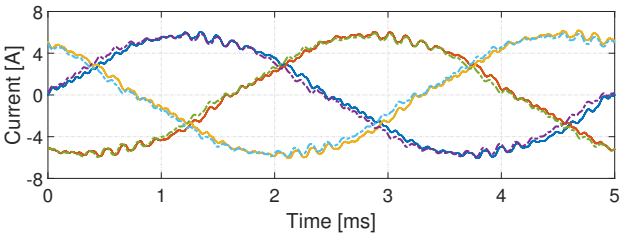

(j) Waveforms: $f_o = 200$ Hz, $p = 36$, 60 μF, $V_{dc} = 33$ V, $M = 0.8$.

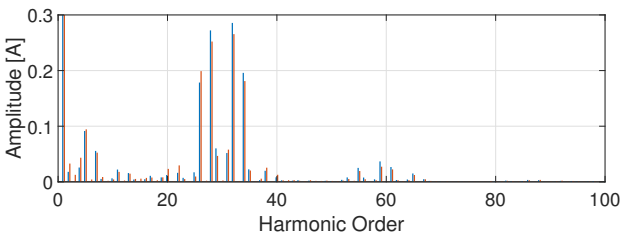

(k) Spectra: $f_o = 400$ Hz, $p = 30$, 10 μF, $V_{dc} = 50$ V, $M = 1.0$.

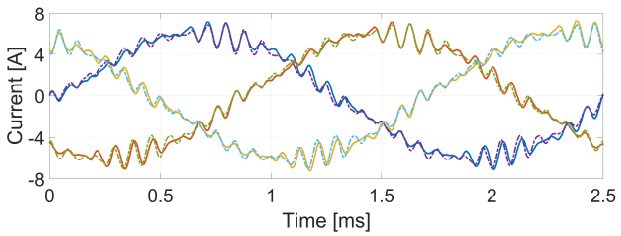

(l) Waveforms: $f_o = 400$ Hz, $p = 30$, 10 μF, $V_{dc} = 50$ V, $M = 1.0$.

Fig. 17. Predicted and Measured Current Waveforms and Spectra

This article has been accepted for publication in IEEE Transactions on Energy Conversion. This is the author's version which has not been fully edited and content may change prior to final publication. Citation information: DOI 10.1109/TEC.2023.3337191

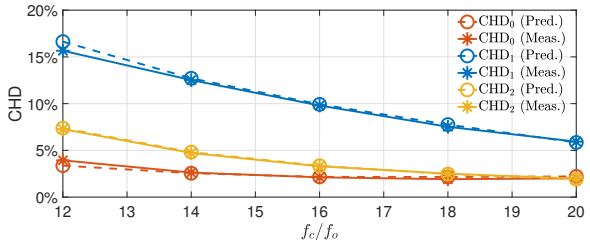

(a) CHD vs. f_c or p ($f_o = 400$ Hz, 60 μF, $V_{dc} = 60$ V, $M = 0.8$)

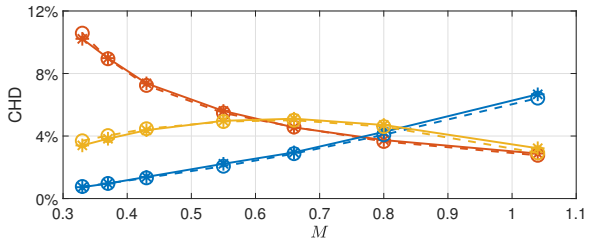

(b) CHD vs. M ($f_o = 100 - 400$ Hz, $f_c = 12$ kHz, 60 μF, $V_{dc} = 50$ V)

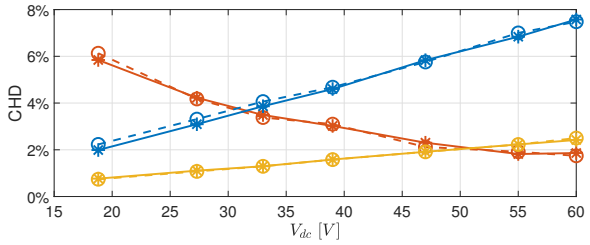

(c) CHD vs. V_{dc} ($f_o = 200 - 400$ Hz, $f_c = 7.2$ kHz, 60 μF, $M = 0.8$)

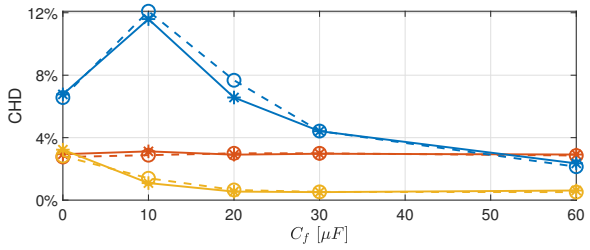

(d) CHD vs. C_f ($f_o = 400$ Hz, $f_c = 12$ kHz, $V_{dc} = 50$ V, $M = 1.0$)

Fig. 18. CHD Trends

attributed to the fact that high-amplitude voltage harmonics are always distributed near integer multiples of the carrier frequency. Therefore, the higher the carrier frequency, the higher the frequencies of high-amplitude voltage harmonics, and the larger the impedance corresponding to those harmonics. This results in lower amplitude of current harmonics. As such, we observe a clear negative correlation between the carrier ratio and harmonic amplitude, as depicted in Fig. 18a, which plots the variations of CHD_0 to CHD_2 in the range of p, or the normalized f_c with f_o, from 12 to 20.

Our experimental results demonstrate that all three CHDs exhibit decreasing trend with respect to a rising f_c. We note that this observation is in excellent agreement with our predicted values. Given the significant influence of f_c on the current harmonic amplitudes, we maintain f_c constant when analyzing the effects of other parameters in the following tests.

C. Modulation Index

Figs. 17e-17h illustrate the spectra and waveforms of two different M. Here, we switched to using an L filter, raised the f_c to 12 kHz and kept V_{dc} at 50 V. In the Figs. 17e and 17f case, f_o is 200 Hz and $M = 0.55$. In the Figs. 17g and 17h case, f_o is 400 Hz and $M = 1.0$.

When $M = 0.55$, the amplitude of the second carrier sideband-group harmonics is higher than that of the first carrier sideband-group harmonics. However, when $M = 1.0$, the opposite is true. This is because M has a different effect on the harmonics belonging to these two individual sideband-groups. As shown in Fig. 18b, CHD_1 monotonically increases with M, while CHD_2 first increases and then decreases. In general, the higher the value of M, the higher the harmonic content of the first sideband. Because the impedance corresponding to lower carrier order is smaller, THD is also higher for higher M.

It is worth noting that the switch dead time results in high-amplitude components in the baseband harmonic group. The voltage distortion component of dead time is generally proportional to f_c and V_{dc}, while the corresponding impedance is proportional to f_o. Therefore, as M decreases and f_o becomes lower, CHD_0 becomes larger. The distorted waveforms caused by dead time are also more clearly visible in Fig. 17f.

Furthermore, the good agreement between prediction and test results shows that the proposed analytical method is valid for motor drive systems with both LC and L filters. This shows the method's versatility even with high-order circuits.

D. Dc Bus Voltage

Keeping f_c and M constant, influence of V_{dc} is studied. By reducing V_{dc} of the Fig. 17a case from 60 V to 33 V and f_o from 400 Hz to 200 Hz, we obtain the spectrum and waveforms in Figs. 17i and 17j. f_c and M are kept at 7.2 kHz and 0.8, respectively. The shapes of the spectra in these two cases are almost the same. The major difference is that all harmonics in the 33-V case have about half amplitudes of those in the 60-V case. This is because the PWM voltage harmonic amplitudes are directly proportional to V_{dc}. Under the same f_c, M, and system impedance, current harmonic amplitudes should follow the same linear relationship.

Fig. 18c shows the trend of CHD with respect to V_{dc}. CHD_1 and CHD_2 increase almost linearly with V_{dc}, consistent with theoretical predictions. However, CHD_0 shows the opposite trend due to lower dead-time distortion at higher f_o.

E. Filter Capacitance

The influence of C_f variation on the current spectrum is investigated. First, we compare the cases with and without C_f. In the L-filtered case of Fig. 17g, adding a 10 μF capacitance changes the system to an LC-filtered case and the results are shown in Figs. 17k and 17l. The system now has a higher f_{res} of 13.8 kHz, while f_c is 12 kHz. The first carrier-sideband-group harmonics will excite the resonant mode when $f_c < f_{\mathrm{res}}$. The amplitude of current harmonics is even higher than the that of the case when no capacitor is added. The second carrier-group harmonics are farther from f_{res}, so the high-frequency harmonic components in the current waveforms are

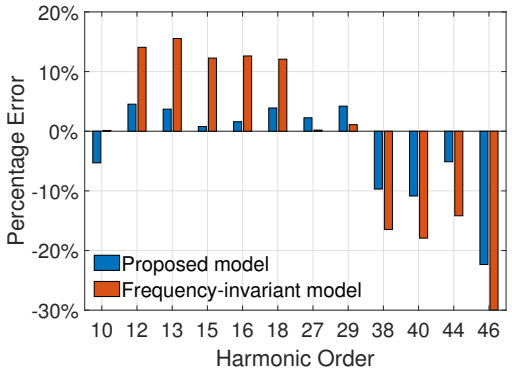

(a) Fig. 17c Case

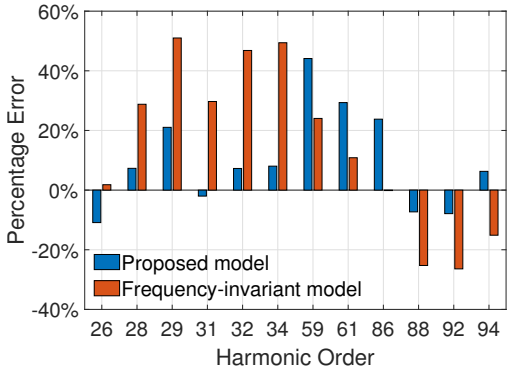

(b) Fig. 17k Case

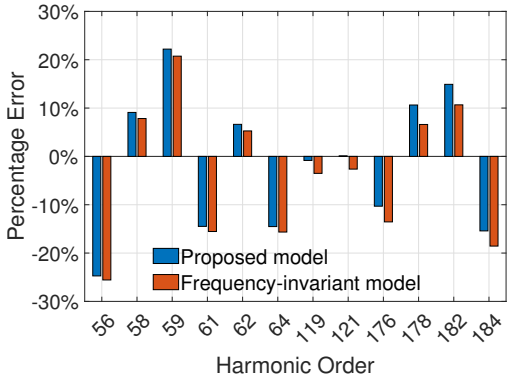

(c) Fig. 17e Case

Fig. 19. Prediction Error Comparison for Significant Carrier Harmonics

bypassed through the shunt C_f, resulting in a decrease in the second carrier-sideband-group harmonics.

Fig. 18d shows the trend of CHD_m for C_f ranging from 0 to 60 μF. When we increase C_f further beyond 10 μF, f_{res} decreases and moves away from f_c. Therefore, CHD_1 curve decreases with an increase in C_f. Meanwhile, the larger the C_f, the stronger its filtering effect, resulting in a lower CHD_2. Thus, as long as f_{res} is substantially lower than f_c, adding filter capacitance is an effective means to reduce the current harmonics. As p remains constant at 30, dead-time distortion does not change much, CHD_0 curve is almost flat.

F. Sideband Carrier Harmonic Prediction Error

Next, we will compare the prediction errors between the improved model we proposed and the original frequency-invariant model. We define individual harmonic prediction error in relative percentage as

$$P.E.\,(h) = \frac{I_h^{\mathrm{Pred}} - I_h^{\mathrm{Meas.}}}{\left|I_h^{\mathrm{Meas.}}\right|} \times 100\%. \tag{34}$$

$P.E.\,(h)$ can be used to demonstrate the prediction error distribution over the frequency spectrum to identify any systematic prediction errors and analyze their patterns. The root mean squared (rms) weighted prediction error in relative percentage for all significant harmonics is defined as

$$P.E._{\mathrm{rms}} = \sqrt{\frac{\sum_h \left|I_h^{\mathrm{Pred.}} - I_h^{\mathrm{Meas.}}\right|^2}{\sum_h \left|I_h^{\mathrm{Meas.}}\right|^2}} \times 100\%, \tag{35}$$

where h shall take all corresponding ordinals to significant harmonics, i.e., $h = p \pm 1, p \pm 2, p \pm 4, 2p \pm 1, 3p \pm 2$. $P.E._{\mathrm{rms}}$ is equivalently a weighted average gauge that provides a good measure of the overall harmonic prediction accuracy and can be used to compare different scenarios.

Fig. 19 illustrates the $P.E.\,(h)$ distribution of the two models under three different cases. From cases (a) and (b), the original frequency-invariant model clearly exhibits systematic prediction errors, which overestimates harmonics around the resonant frequencies and underestimates them at high frequencies, aligning with our earlier impedance observations. In contrast, the proposed model effectively reduces such prediction errors. In the high-order harmonic range, the proposed model might also exhibit relatively large errors, which can be attributed to the inherently low amplitudes in this frequency range. Low-amplitude harmonics are more susceptible to external dynamic disturbances and more difficult to measure precisely. In case (c), where no capacitor is present and the equivalent circuit only consists of a large filter inductor in series with the motor, the frequency-dependent effects on the overall impedance have been diluted. Here, harmonic prediction errors mainly arise from an imperfect modeling of the PWM voltage spectrum.

TABLE V presents the rms prediction error in relative percentage across various scenarios. In cases corresponding to LC filtered configuration, the original frequency-invariant model, due to the lack of frequency effect consideration, may yield prediction errors up to 36.7%. The proposed model notably enhances prediction accuracy by modeling the frequency effect. The reduction rate of relative percentage error is between 25.9% to 75.7%. In cases corresponding to L-filtered configuration, frequency effect is limited and our model provides modest improvement by 7–10%. Overall, the prediction error is generally maintained below 10% with the proposed model, indicating a satisfactory prediction accuracy for practical applications. These comparative results underscore the effectiveness of the proposed method and its significant improvement compared to the conventional model.

V. Conclusion

This paper presents an analytical current harmonic prediction method for slotless surface-mounted PMSMs. The spectral prediction is performed directly in the frequency domain using double-integral Fourier coefficients and a sequence-harmonic

TABLE V
RMS PREDICTION ERROR COMPARISON FOR SIGNIFICANT CARRIER HARMONICS

	Filter Type	Dominant carrier harmonic frequency [kHz]	RMS Prediction Error [%] Proposed model	Frequency-invariant model	Error reduction
Fig. 17a case	LC	7.2	13.0	17.6	-25.9%
Fig. 17c case	LC	5.6	4.3	12.6	-65.9%
Fig. 17e case	L	24	6.9	7.5	-7.7%
Fig. 17g case	L	12	8.4	9.4	-10.6%
Fig. 17i case	LC	7.2	7.7	11.7	-34.5%
Fig. 17k case	LC	12	8.9	36.7	-75.7%

equivalent circuit model. The model incorporates impedance-frequency characteristics of each circuit component, thus giving rise to an accurate representation of the Thevenin equivalent impedance. The influence of carrier frequency, modulation index, dc bus voltage, and filter capacitance on the various sideband harmonics is predicted, and validated with experimental results. A comparison has been made on the prediction errors from the proposed model and the conventional frequency-invariant circuit model. The proposed model comprehensively reduces prediction errors, and in certain scenarios, prediction accuracy can be improved by 70%.

APPENDIX

The Fourier coefficients A_{mn} for voltage harmonics with regularly-sampled, symmetrical carrier SVPWM is given by [29]as

$$
\begin{aligned}
&A_{mn} = \frac{8}{q\pi^2}\cdot \\
&\left[\frac{\pi}{6}\left(\sin[q+n]\frac{\pi}{2}\right)\left\{J_n\left(q\frac{3\pi}{4}M\right)+2\cos n\frac{\pi}{6}J_n\left(q\frac{\sqrt{3}\pi}{4}M\right)\right\}\right. \\
&\left.+\frac{1}{n}\sin q\frac{\pi}{2}\cos n\frac{\pi}{2}\sin n\frac{\pi}{6}\left\{J_0\left(q\frac{3\pi}{4}M\right)-J_0\left(q\frac{\sqrt{3}\pi}{4}M\right)\right\}\right|_{n\neq 0} \\
&+\sum_{\substack{k=1\\(k\neq -n)}}^{\infty}\left[\begin{array}{l}\frac{1}{[n+k]}\sin\left([q+k]\frac{\pi}{2}\right)\cos\left([n+k]\frac{\pi}{2}\right)\sin\left([n+k]\frac{\pi}{6}\right)\\ \times\left\{J_k\left(q\frac{3\pi}{4}M\right)+2\cos\left([2n+3k]\frac{\pi}{6}\right)J_k\left(q\frac{\sqrt{3}\pi}{4}M\right)\right\}\end{array}\right] \\
&+\sum_{\substack{k=1\\(k\neq n)}}^{\infty}\left[\begin{array}{l}\frac{1}{[n-k]}\sin\left([q+k]\frac{\pi}{2}\right)\cos\left([n-k]\frac{\pi}{2}\right)\sin\left([n-k]\frac{\pi}{6}\right)\\ \times\left\{J_k\left(q\frac{3\pi}{4}M\right)+2\cos\left([2n-3k]\frac{\pi}{6}\right)J_k\left(q\frac{\sqrt{3}\pi}{4}M\right)\right\}\end{array}\right],
\end{aligned}
\tag{36}
$$

where J_n is the Bessel functions of the first kind, and $q = m + \frac{n}{p}$. For asymmetrical carrier SVPWM and various other PWM schemes, analytical expressions for A_{mn} can also be found in [29].

REFERENCES

[1] X. Zhang and K. S. Haran, "High-specific-power electric machines for electrified transportation applications-technology options," in *Proc. IEEE Energy Convers. Congr. Expo.*, Oct. 2016, pp. 1–8.

[2] Z. Song, C. Liu, and H. Zhao, "Comparative analysis of slotless and coreless permanent magnet synchronous machines for electric aircraft propulsion," in *Proc. Int. Conf. Electr. Mach. Systems*. IEEE, Aug. 2019, pp. 1–6.

[3] M. S. Islam, R. Mikail, and I. Husain, "Slotless lightweight motor for aerial applications," *IEEE Trans. Ind. Applicat.*, vol. 55, no. 6, pp. 5789–5799, 2019.

[4] P. H. Mellor, C. Heath, S. Collins, N. Simpson, and I. Bond, "Addressing the challenges of lightweight aircraft electric propulsion through electrical machines with air-gap windings," in *Proc. IEEE Energy Convers. Congr. Expo.*, Sep. 2019, pp. 4470–4476.

[5] D. Lawhorn, P. Han, D. Lewis, Y. Chulaee, and D. M. Ionel, "On the design of coreless permanent magnet machines for electric aircraft propulsion," in *Proc. IEEE Transport. Electrific. Conf. and Expo.*, Jun. 2021, pp. 278–283.

[6] R. Sanchez, A. Yoon, X. Yi, L. Zheng, Y. Chen, K. S. Haran, A. Provenza, and J. Veres, "Mechanical validation of a high power density external cantilevered rotor," *IEEE Trans. Ind. Applicat.*, vol. 54, no. 4, pp. 3208–3216, 2018.

[7] S. G. Min, "Modeling, investigation, and minimization of AC winding loss in slotless PM machines," *IEEE Trans. En. Conv.*, vol. 36, no. 3, pp. 2249–2260, 2021.

[8] M. G. Granger, A. Anderson, J. M. Maroli, T. Tallerico, and J. J. Scheidler, "Combined analysis of NASA's high efficiency megawatt motor and its converter," in *Proc. AIAA Propulsion and Energy 2021 Forum*, p. 3276.

[9] W. Geng, Z. Zhang, and Q. Li, "Analysis and experimental verification of a conventional inverter with output LC filter to drive ironless stator axial-flux PM motor," *IEEE Trans. Transport. Electrific.*, 2021.

[10] M. G. Granger, D. Avanesian, R. Jansen, S. R. Kowalews i, A. Leary, R. Bowman, A. Dimston, E. Stalcup, and W. A. Miller, "Design of a high power density, high efficiency, low THD 250 kW converter for electric aircraft," in *Proc. AIAA Propulsion and Energy 2021 Forum*, p. 3332.

[11] C.-C. Hsu, S.-C. Yang, and J.-Y. Chen, "Implementation of low inductance permanent magnet machine drive with LC filter for field oriented control," in *Proc. IEEE Energy Convers. Congr. Expo.* IEEE, Sep. 2019, pp. 6140–6146.

[12] M. Leandro, N. Bianchi, M. Molinas, and R. B. Ummaneni, "Low inductance effects on electric drives using slotless permanent magnet motors: A framework for performance analysis," in *Proc. IEEE Int. Electr. Mach. Drives Conf.*, May 2019, pp. 1099–1105.

[13] K. Yamazaki and A. Abe, "Loss investigation of interior permanent-magnet motors considering carrier harmonics and magnet eddy currents," *IEEE Trans. Ind. Applicat.*, vol. 45, no. 2, pp. 659–665, 2009.

[14] K. Yamazaki, Y. Togashi, T. Ikemi, S. Ohki, and R. Mizokami, "Reduction of inverter carrier harmonic losses in interior permanent magnet synchronous motors by optimizing rotor and stator shapes," *IEEE Trans. Ind. Applicat.*, vol. 55, no. 1, pp. 306–315, 2018.

[15] M. Cheng and S. Zhu, "Calculation of PM eddy current loss in IPM machine under PWM VSI supply with combined 2-D FE and analytical method," *IEEE Trans. Magn.*, vol. 53, no. 1, pp. 1–12, 2016.

[16] T.-C. Jeong, W.-H. Kim, M.-J. Kim, K.-D. Lee, J.-J. Lee, J.-H. Han, T.-H. Sung, H.-J. Kim, and J. Lee, "Current harmonics loss analysis of 150-kW traction interior permanent magnet synchronous motor through co-analysis of *dq* axis current control and finite element method," *IEEE Trans. Magn.*, vol. 49, no. 5, pp. 2343–2346, 2013.

[17] A. G. Sarigiannidis and A. G. Kladas, "Switching frequency impact on permanent magnet motors drive system for electric actuation applications," *IEEE Trans. Magn.*, vol. 51, no. 3, pp. 1–4, 2015.

[18] R. Sprangers, J. Paulides, B. Gysen, E. Lomonova, and J. Waarma, "Electric circuit coupling of a slotted semi-analytical model for induction motors based on harmonic modeling," in *Proc. IEEE Energy Convers. Congr. Expo.*, Sep. 2014, pp. 1301–1308.

[19] S. Jumayev, M. Merdzan, K. Boynov, J. Paulides, J. Pyrhönen, and E. Lomonova, "The effect of PWM on rotor eddy-current losses in high-speed permanent magnet machines," *IEEE Trans. Magn.*, vol. 51, no. 11, pp. 1–4, 2015.

[20] D. Smith, S. Lambert, B. Mecrow, and G. Atkinson, "Interaction between PM rotor design and voltage fed inverter output," in *6th IET Int. Conf. Power Electron. Mach. Drives*, Mar. 2012, pp. 1–6.

[21] N. Chiodetto, B. Mecrow, R. Wrobel, and T. Lisle, "Electro-mechanical challenges in the design of a high-speed-high-power-PMSM rotor for an

aerospace application," in *Proc. IEEE Energy Convers. Congr. Expo.*, Sep. 2019, pp. 3944–3951.

[22] S. Zuo, Z. Huang, Z. Wu, and C. Liu, "Improved mathematical model and modeling of permanent magnet synchronous motors considering saturation, spatial harmonics, iron loss and deadtime effect," *Arabian Journal for Science and Engineering*, pp. 1–17, 2023.

[23] J. Ou, Y. Liu, D. Liang, and M. Doppelbauer, "Investigation of PM eddy current losses in surface-mounted PM motors caused by PWM," *IEEE Trans. Power Electron.*, vol. 34, no. 11, pp. 11 253–11 263, 2019.

[24] L. Chang and T. M. Jahns, "Prediction and evaluation of PWM-induced current ripple in IPM machines incorporating slotting, saturation, and cross-coupling effects," *IEEE Trans. Ind. Applicat.*, vol. 54, no. 6, pp. 6015–6026, 2018.

[25] J.-D. Park, C. Khalizadeh, and H. Hofmann, "Design and control of high-speed solid-rotor synchronous reluctance drive with three-phase LC filter," in *Rec. IEEE Ind. Appl. Soc. Annu. Meeting*, vol. 1, Oct. 2005, pp. 715–722.

[26] W. Liang, J. Wang, P. C.-K. Luk, W. Fang, and W. Fei, "Analytical modeling of current harmonic components in PMSM drive with voltage-source inverter by SVPWM technique," *IEEE Trans. En. Conv.*, vol. 29, no. 3, pp. 673–680, 2014.

[27] W. Liang, W. Fei, and P. C.-K. Luk, "An improved sideband current harmonic model of interior PMSM drive by considering magnetic saturation and cross-coupling effects," *IEEE Trans. Ind. Electron.*, vol. 63, no. 7, pp. 4097–4104, 2016.

[28] A. M. Stankovic, S. R. Sanders, and T. Aydin, "Dynamic phasors in modeling and analysis of unbalanced polyphase AC machines," *IEEE Trans. En. Conv.*, vol. 17, no. 1, pp. 107–113, 2002.

[29] D. G. Holmes and T. A. Lipo, *Pulse Width Modulation for Power Converters: Principles and Practice*. John Wiley & Sons, 2003.

[30] S. S. Thakur, M. Odavic, A. Allu, Z. Zhu, and K. Atallah, "Theoretical harmonic spectra of PWM waveforms including DC bus voltage ripple—Application to a low-capacitance modular multilevel converter," *IEEE Trans. Power Electron.*, vol. 35, no. 9, pp. 9291–9305, 2020.

[31] D. C. Moore, M. Odavic, and S. M. Cox, "Dead-time effects on the voltage spectrum of a PWM inverter," *IMA Journal of Applied Mathematics*, vol. 79, no. 6, pp. 1061–1076, 2014.

[32] P. Dowell, "Effects of eddy currents in transformer windings," in *Proc. Inst. Elec. Eng.*, vol. 113, no. 8. IET, 1966, pp. 1387–1394.

[33] T. Jokinen, V. Hrabovcova, and J. Pyrhonen, *Design of Rotating Electrical Machines*. John Wiley & Sons, 2013.

[34] G. Widger and B. Adkins, "Starting performance of synchronous motors with solid salient poles," in *Proc. Inst. Electr. Eng.*, vol. 115, no. 10. IET, 1968, pp. 1471–1484.

[35] I. Canay, "Causes of discrepancies on calculation of rotor quantities and exact equivalent diagrams of the synchronous machine," *IEEE Trans. Power App. Syst.*, no. 7, pp. 1114–1120, 1969.

[36] K. W. Klontz, T. J. Miller, M. I. McGilp, H. Karmaker, and P. Zhong, "Short-circuit analysis of permanent-magnet generators," *IEEE Trans. Ind. Applicat.*, vol. 47, no. 4, pp. 1670–1680, 2011.

[37] O. V. Thorsen and M. Dalva, "Improved model for simulation of saturated deep bar induction motors-application to direct start and start by open-and closed wye-delta transition," in *Rec. IEEE Ind. Appl. Soc. Annu. Meeting*, Oct. 1992, pp. 115–122.

[38] T. A. Lipo, *Introduction to AC Machine Design*. John Wiley & Sons, 2017.